Monthly Notices of the ROYAL ASTRONOMICAL SOCIETY
MNRAS **493,** 3412–3421 (2020) doi:10.1093/mnras/staa481
Advance Access publication 2020 February 20

No nitrogen fractionation on 600 au scale in the Sun progenitor analogue OMC–2 FIR4

F. Fontani ,[1,2]★ G. Quaia,[3] C. Ceccarelli ,[4] L. Colzi,[1,3] A. López-Sepulcre,[4,5] C. Favre,[4] C. Kahane,[4] P. Caselli,[2] C. Codella,[1,4] L. Podio [1] and S. Viti[6]

[1]*INAF-Osservatorio Astrofisico di Arcetri, Largo E. Fermi 5, I-50125, Florence, Italy*
[2]*Centre for Astrochemical Studies, Max-Planck-Institute for Extraterrestrial Physics, Giessenbachstrasse 1, D-85748 Garching, Germany*
[3]*Dipartimento di Fisica e Astronomia, Università degli Studi di Firenze, I-50125 Firenze, Italy*
[4]*IPAG, Université Grenoble Alpes, CNRS, F-38000 Grenoble, France*
[5]*Institut de Radioastronomie Millimétrique, 300 rue de la Piscine, Domaine Universitaire de Grenoble, 38406, Saint-Martin d'Hères, France*
[6]*Department of Physics and Astronomy, UCL, Gower St., London WC1E 6BT, UK*

Accepted 2020 February 14. Received 2020 February 14; in original form 2019 June 14

ABSTRACT

We show the first interferometric maps of the ^{14}N/^{15}N ratio obtained with the Atacama Large Millimeter Array (ALMA) towards the Solar-like forming protocluster OMC–2 FIR4. We observed N_2H^+, $^{15}NNH^+$, $N^{15}NH^+$ (1–0), and N_2D^+(2–1) from which we derive the isotopic ratios ^{14}N/^{15}N and D/H. The target, OMC–2 FIR4, is one of the closest analogues of the environment in which our Sun may have formed. The ALMA images, having synthesized beam of ∼1.5 arcsec × 1.8 arcsec, i.e. ∼600 au, show that the emission of the less abundant isotopologues is distributed in several cores of ∼10 arcsec (i.e. ∼0.02 pc or 4000 au) embedded in a more extended N_2H^+emission. We have derived that the ^{14}N/^{15}N ratio does not vary from core to core, and our interferometric measurements are also consistent with single-dish observations. We also do not find significant differences between the ^{14}N/^{15}N ratios computed from the two ^{15}N-bearing isotopologues, $^{15}NNH^+$ and $N^{15}NH^+$. The D/H ratio derived by comparing the column densities of $N_2D^+$and N_2H^+changes by an order of magnitude from core to core, decreasing from the colder to the warmer cores. Overall, our results indicate that: (1) ^{14}N/^{15}N does not change across the region at core scales, and (2) ^{14}N/^{15}N does not depend on temperature variations. Our findings also suggest that the ^{14}N/^{15}N variations found in pristine Solar system objects are likely not inherited from the protocluster stage, and hence the reason has to be found elsewhere.

Key words: Stars: formation – ISM: clouds – ISM: molecules.

1 INTRODUCTION

One of the unsolved mysteries about the Solar system is why the nitrogen isotopic ratio, $R = {}^{14}$N/^{15}N, was ∼440 in the Proto Solar Nebula (PSN, Owen et al. 2001; Fouchet et al. 2004; Marty et al. 2010), while now it is ∼270 in the Earth atmosphere (Marty, Zimmermann & Burnard 2009), ∼140 in comets (Manfroid et al. 2009; Shinnaka et al. 2016), and 50–300 in the insoluble organic matter (e.g. Bonal et al. 2009; Matrajt et al. 2012; Nittler et al. 2018) and soluble organic compounds (e.g. Pizzarello & Holmes 2009; Chan et al. 2014; Pizzarello 2014) of meteorites. What causes such variations was (and still is) puzzling astronomers and cosmochemists for decades. It is now clear that there are up to three different reservoirs of nitrogen in the Solar system, which have distinct N isotopic ratios (see, for example, the discussion in Füri & Marty 2015): the PSN, where $R \sim 440$; the inner Solar system, in which planets and bulk meteorites appear enriched in ^{15}N by a factor ∼1.6 with respect to the PSN; and the cometary ices, enriched up to a factor of ∼3 relative to the PSN, although the inner Solar system reservoir could be a mixture of the two 'extreme' values: the Sun and the cometary material. Nonetheless, it remains the question of what causes the relatively large range of R in cometary and meteoritic material, and whether this has an ISM origin.

One popular explanation for the nitrogen isotopic fractionation has been that, as for the hydrogen isotopic one, it has to be attributed to (low) temperature effects (Terzieva & Herbst 2000; Rodgers & Charnley 2008; Furuya & Aikawa 2018). However, several theoretical studies have excluded low-temperature isotopic exchange reactions as the main way to enhance ^{15}N in molecular species (e.g. Wirström et al. 2012; Roueff, Loison & Hickson 2015; Wirström & Charnley 2018; Loison et al. 2019). At odd with theory,

★ E-mail: fontani@arcetri.astro.it

some observations of cold prestellar and protostellar objects seem to show variations of one order of magnitude (∼100–1000) in the N isotopic ratio, which even depends on the used molecule (Womack, Ziurys & Wyckoff 1992; Caselli & Ceccarelli 2012; Bizzocchi et al. 2013; Daniel et al. 2013; Hily-Blant et al. 2013; Fontani et al. 2015a; Daniel et al. 2016; Guzmán et al. 2017; Hily-Blant et al. 2017; Zeng et al. 2017; Colzi et al. 2018a; De Simone et al. 2018; Redaelli et al. 2018).

Kahane et al. (2018), see also De Simone et al. (2018), obtained large-scale (∼10 000 au) high-precision observations of the five brightest N-bearing molecules (HCN, HNC, CN, HC_3N, and N_2H^+) towards one of the best known analogue of the environment in which the Solar system was born, OMC–2 FIR4. They derived the same *R* value, ∼270, in all the five molecules, regardless on the CN- or NH-bond. This measured value is slightly lower than the most recent estimate in the interstellar medium nowadays (375 ± 60, Colzi et al. 2018a), although measurements in the local ISM show a large spread of values (Hily-Blant et al. 2017, and reference therein). However, these single-dish measurements provide average values over ∼10 000 au, namely on the whole protocluster, so that it cannot exclude the presence of local spots enriched (or depleted) in ^{15}N. In fact, differences of a factor of 2 on *R* can be measured from N_2H^+ when *R* is measured on angular scales that can resolve the dense cores from the extended, diffuse envelope, as found by Colzi et al. (2019) in a high-mass protocluster.

In order to address this possibility, we obtained new ALMA observations towards OMC–2 FIR4 of N_2H^+, $^{15}NNH^+$, and $N^{15}NH^+$ lines with a spatial resolution of about 600 au. We simultaneously also observed the N_2H^+ deuterated form, N_2D^+, which provides a sort of reference for isotope fractionation due to temperature.

This paper is organized as follows. The OMC–2 FIR4 background is reported in Section 2; the observations are described in Section 3; and the results are presented in Section 4, and discussed in Section 5, where we also give the main conclusions of this paper.

2 SOURCE BACKGROUND

The target of this work is the young protocluster OMC–2 FIR4 in the Orion star-forming region, at a distance of 388 ± 5 pc (Kounkel et al. 2017). It lies in between two other young protostars: FIR3 (also known as SOF 2N or HOPS 370, Adams et al. 2012), about 30 arcsec north-west, and FIR5 (SOF 4 or HOPS 369, Adams et al. 2012), about 20 arcsec south-east (Mezger, Zylka & Wink 1990). OMC–2 FIR4 is itself a young protocluster that harbours several embedded low- and intermediate-mass protostars (Shimajiri et al. 2008; López-Sepulcre et al. 2013). Its unicity is due to the fact that observations have suggested the exposition of OMC–2 FIR4 to a dose of energetic particles very similar to that experienced by the young Solar system. Although the source of these energetic particles is still under debate, and it is not clear if they are originated in the cluster itself from nascent protostars, or from nearby external sources (Fontani et al. 2017; Osorio et al. 2017), such energetic irradiation responsible for an enhanced cosmic ray ionization rate was confirmed by three independent studies (Ceccarelli et al. 2014a; Fontani et al. 2017; Favre et al. 2018). This and the increasing evidence that the Sun was born in a crowded cluster of stars rather than in an isolated clump (Adams 2010; Lichtenberg et al. 2019) make OMC–2 FIR4 one of the best and closest analogues of what must have been the environment of our Sun at the very beginning of its formation. In this context, the study of the N isotopic fractionation towards OMC–2 FIR4 provides constraints on the N isotopic fractionation in an environment similar to the one in which our Sun may have been born.

3 OBSERVATIONS

Observations towards OMC–2 FIR4 using 40 antennas of the Atacama Large Millimeter Array (ALMA) in Cycle 4 were carried out as part of the project 2016.1.00681.S (PI: F. Fontani), in band 3 (3 mm) in 2016 December 23–25, and in band 4 (2 mm) in 2017 March 11. The correlator was configured in four different spectral windows to cover lines of N_2H^+, $^{15}NNH^+$, $N^{15}NH^+$ (1–0) at 3 mm, and N_2D^+(2–1) at 2 mm. Relevant spectral parameters are given in Table 1. Flux and bandpass calibration were obtained through observations of J0423-0120. Visibility phases and amplitudes were calibrated on quasar J0541-0541. Some important observational parameters (baseline range, precipitable water vapour, system temperature, on-source total observing time, synthesized beam, and spectral resolution) are reported in Table 1. The coordinates of the phase centre were RA = $05^h35^m27.''0$, Dec = $-05°09'56.''8$.

The data were calibrated using standard ALMA calibration scripts of the Common Astronomy Software Applications (CASA,[1] version 4.7.0) package. The calibrated data cubes were converted in fits format and analysed in GILDAS[2] format and then imaged and deconvolved with software MAPPING of the GILDAS package using standard procedures. Continuum subtraction was performed by taking the line-free channels around the lines in each individual spectral window and subtracted from the data directly in the (*u,v*) domain. The nominal maximum recoverable scale (MRS) was ∼25 arcsec in band 3 and ∼19 arcsec in band 4.

4 RESULTS

The N_2H^+, $^{15}NNH^+$, and $N^{15}NH^+$ (1–0) lines, and the N_2D^+(2–1) line, were all clearly detected towards OMC–2 FIR4. The maps of their intensity averaged over the full-line profiles are shown in Fig. 1. As reference, in the same plot, we show the 82-GHz continuum map published by Fontani et al. (2017). We do not show the ALMA continuum maps obtained from the data set presented in Section 3 because a high-angular resolution map of the continuum is not crucial for the analysis we make in this work, and a study totally devoted to the continuum emission will be presented in a forthcoming paper (Neri et al. in preparation).

We detect significant emission over an angular region as extended as ∼30 arcsec in N_2H^+ and up to ∼20 arcsec in N_2D^+. In particular, N_2H^+ shows two main intensity peaks separate by ∼15 arcsec in the east–west direction, embedded in an irregular diffuse envelope, while N_2D^+ is concentrated in two cores partly overlapping along a north–south direction, whose peaks are separated by ∼10 arcsec. The extension of the N_2H^+ and N_2D^+ maps overall overlaps well with that of the mm continuum. The rough angular size of each core is smaller than the nominal MRS (see Section 3) of its observing band. The most intense N_2D^+ core coincides with the strongest N_2H^+ emission peak, while the second one is offset by ∼10

[1] CASA is developed by an international consortium of scientists based at the National Radio Astronomical Observatory (NRAO), the European Southern Observatory (ESO), the National Astronomical Observatory of Japan (NAOJ), the Academia Sinica Institute of Astronomy and Astrophysics (ASIAA), the CSIRO division for Astronomy and Space Science (CASS), and the Netherlands Institute for Radio Astronomy (ASTRON) under the guidance of NRAO.
[2] https://www.iram.fr/IRAMFR/GILDAS/

Table 1. Observational and spectroscopic parameters of the observed lines.

Band–molecule	Baseline range (m)	T_{sys} (K)	pwv (mm)	Int. time (min)	θ_{SB} ($''$)	$1\sigma^{a}$ (mJy)
3 – N_2H^+	15–491	50–130	3.2	136	1.5 × 1.8	∼1.5
3 – $^{15}NNH^+$	15–491	50–100	3.2	136	1.5 × 1.8	∼1.2
3 – $N^{15}NH^+$	15–491	50–100	3.2	136	1.5 × 1.8	∼1.2
4 – N_2D^+	15–321	60–100	3.1	32	1.4 × 1.8	∼3
Bandwidth	Transition	Rest ν^{b} (GHz)	$E_u{}^{b}$ (K)	$S_{ij}\mu^{2b}$ (D^2)	$A_{ij}{}^{b}$ (s^{-1})	ΔV^{c} (km s^{-1})
93.14–93.22	N_2H^+ (1–0)	93.173402	4.47	104	3.6×10^{-5}	∼0.2
90.21–90.32	$^{15}NNH^+$ (1–0)	90.263833	4.33	35	3.3×10^{-5}	∼0.4
91.15–21.26	$N^{15}NH^+$ (1–0)	91.205695	4.47	35	3.4×10^{-5}	∼0.4
154.15–154.38	N_2D^+ (2–1)	154.217011	11.1	208	5.9×10^{-4}	∼0.2

[a]Root mean square (rms) noise per channel in each spectral window.
[b]Taken from the Cologne Molecular Database for Spectroscopy (CDMS; Endres et al. 2016).
[c]Spectral resolution.

arcsec to the north of the main one, detected also in N_2H^+but less prominent. The N_2H^+emission is more intense towards the western and southern portion of the protocluster, and a slight asymmetry with respect to the continuum can be noticed, as also found by Colzi et al. (2019) in the first (and unique so far) interferometric study of R from N_2H^+towards the high-mass protocluster IRAS 05358 + 3543. A filamentary N_2H^+feature connects FIR4 to FIR5 towards the south. This structure is present also in the continuum emission.

The ^{15}N isotopologues show emission much more compact than that of N_2H^+. This could just be the consequence of the (almost) uniform sensitivity we achieved in both the main and rare isotopologues, which likely prevents the detection of the fainter rare isotopologues in the more diffuse envelope. Overall, the two ^{15}N-isotopologues show a very similar morphology. They both mostly arise from the western portion of FIR4. Significant emission ($\geq 3\sigma$ rms) is also detected towards FIR5. Because the nature of FIR5 is still unclear, and it is not the target of the current work, this source will be discussed in a forthcoming paper presenting more extensively the ALMA data set. To better compare the emission morphology of all N_2H^+isotopologues, in Fig. 2 we superimpose the average map of the emission integrated over the profile of the $F = 0$–1 hyperfine component of N_2H^+: even though the overall morphology is similar, clearly the rare isotopologues are not detected towards the diffuse N_2H^+ emission.

We have checked if we miss some extended flux by extracting spectra from a circular region corresponding to the single-dish beam of the observations presented by Kahane et al. (2018): we recover the whole flux in the ^{15}N isotopologues, and we miss at most 10 per cent of extended flux in N_2H^+(1–0), which is comparable to the uncertainty on the flux calibration. Hence, we can conclude that our analysis is not affected by any significant extended emission resolved out. The fact that there is not extended emission in N_2H^+ in OMC–2 FIR4 makes it peculiar with respect to similar clustered star-forming regions (e.g. Henshaw et al. 2014), in which very often interferometric N_2H^+ emission maps suffer from extended flux resolved out. We speculate that this could be due to a very efficient destruction of N_2H^+ in the external layers, perhaps due to the high irradiation by cosmic rays, known to affect the chemistry of the envelope of the OMC–2 FIR4 from different observational evidence (Ceccarelli et al. 2014a; Fontani et al. 2017; Favre et al. 2018).

The complexity of the emission morphology in all lines makes it difficult to divide OMC–2 FIR4 in well-separated structures. Therefore, we have manually identified five 'coarse' regions defined in a very schematic way: their borders contain one dominant intensity peak of one isotopologue and follow as much as possible the contours of one of the average maps of the rare isotopologues shown in Figs 1 and 2. More specifically:

(i) 'FIR4-east' and 'FIR4-west' contain the two intensity peaks resolved in N_2H^+, and the borders follow roughly the 3σ rms contour of the average $^{15}NNH^+$ and $N^{15}NH^+$ (1–0) emission maps.

(ii) 'FIR4-peak' includes the most intense intensity peak seen in N_2D^+ and roughly follows its 15σ rms contour to well separate this peak to the secondary one.

(iii) 'FIR4-north' includes the less intense N_2D^+emission peak located ∼10 arcsec north of the main one and roughly follows its 15σ rms contour.

(iv) 'FIR4-tot' coincides with the union of regions 'FIR4-east', 'FIR4-west', and 'FIR4-peak' and encompasses roughly the bulk of both $^{15}NNH^+$ and $N^{15}NH^+$ emission.

The spectra of N_2H^+, $^{15}NNH^+$, and $N^{15}NH^+$ (1–0) in flux density unit, and the N_2D^+(2–1) spectrum in brightness temperature unit, extracted from these regions are shown in Fig. 3. The conversion between flux density units and brightness temperature units for N_2D^+has been performed according to the equation: $T_{SB} = 1.222 \times 10^3 F_\nu/(\nu^2\theta_s^2)$, where ν is the observing frequency in GHz units and θ_s is the angular source size, in arcsecond units, defined as the diameter of the circular region having the same area of the core considered. We display different y-axis units for the different isotopologues because of the different methods used to derive R and D/H, which will be discussed in the following sections.

4.1 ^{14}N/^{15}N

From the N_2H^+, $^{15}NNH^+$, and $N^{15}NH^+$ (1–0) spectra shown in Fig. 3, we have first derived the ^{14}N/^{15}N ratios, R, following this approach: we have divided the flux density peak of the $F_1 = 0$–1 hyperfine component of N_2H^+(1–0), with rest frequency 93.17613 GHz, by that of the $F = 0$–1 one of both $^{15}NNH^+$ and $N^{15}NH^+$ (1–0), at rest frequencies 90.2645 and 91.2086 GHz, respectively. These components are indicated in Fig. 3. Full spectroscopic parameters of the hyperfine structure of the three lines are given, e.g. in Kahane et al. (2018) and Colzi et al. (2019). If the compared hyperfine

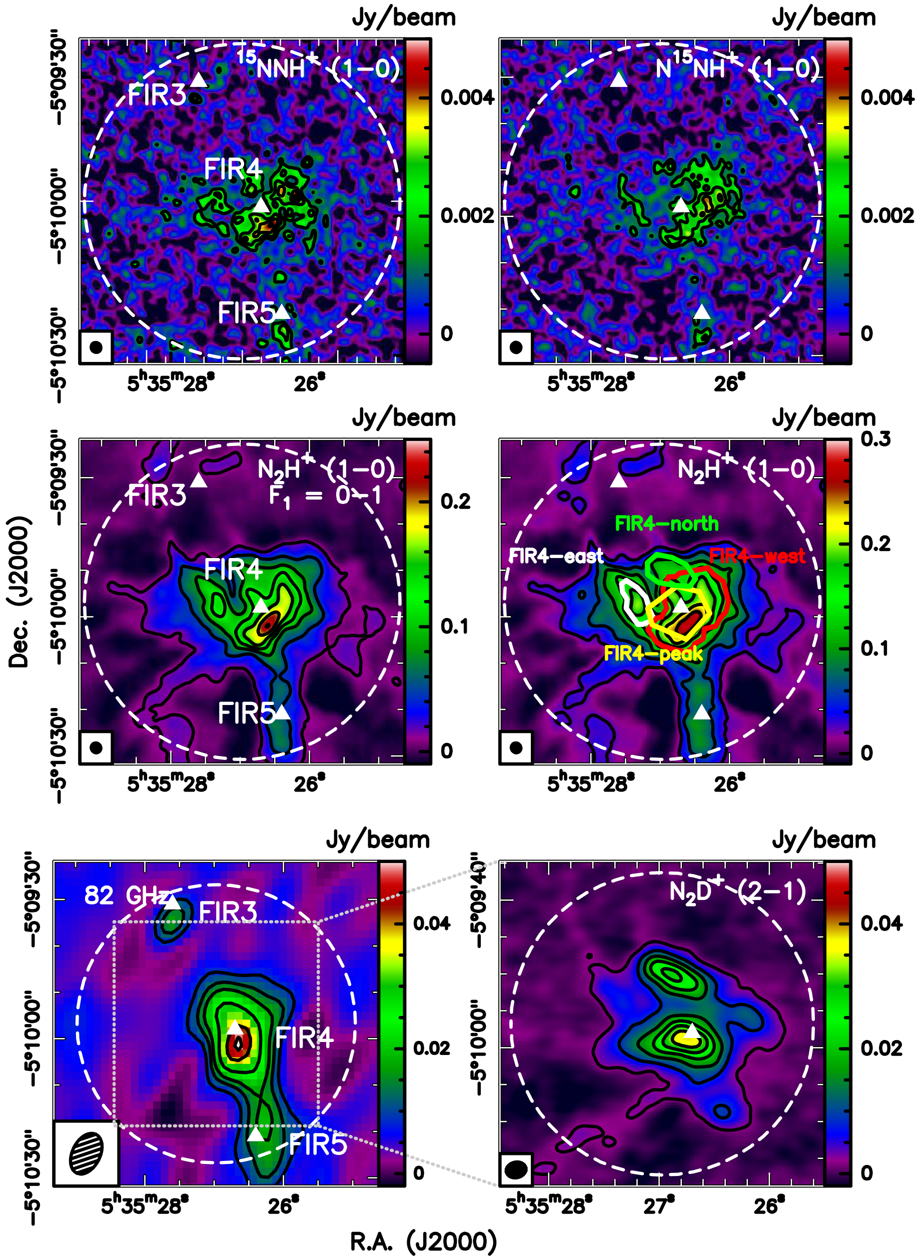

Figure 1. Averaged emission of the N_2H^+ isotopologues studied in this work obtained over the whole line profile, unless when differently specified. The maps show, pixel per pixel, the arithmetic mean of the flux density calculated over the line profiles and are equivalent to the integrated intensity maps, used more often in the literature, when multiplied by the velocity interval (given below) over which the intensity is averaged. *Top panels* (from left to right): $^{15}NNH^+$ (1–0) emission averaged over the velocity range of 8.18–13.72 km s^{-1} (contours start from the 3σ rms level of the averaged map, 1.5 mJy/beam, and are in steps of 1 mJy/beam), and the $N^{15}NH^+$ (1–0) emission averaged over the velocity range of 0.29–19.30 km s^{-1} (first contour and step are the same as in the $^{15}NNH^+$ map). Both velocity ranges include all hyperfine components. Please note that the noise of the average map is equivalent to that of a spectrum smoothed to a spectral resolution equal to the velocity interval covered by the considered channels (hence, much smaller than that of the spectral cube with resolution ~0.4 km s^{-1}, listed in Table 1). *Middle panels* (from left to right): emission on the hyperfine component N_2H^+ (1–0) $F_1 = 0-1$, averaged over the velocity interval 0.38–3.72 km s^{-1} (contours start from 12 mJy/beam, corresponding to the 3σ rms level of the average map, and are in steps of 36 mJy/beam), and total N_2H^+ (1–0) emission averaged over all hyperfine components in the velocity interval 0.38–18.48 km s^{-1}. This plot also shows the four contours in which we have extracted the spectra that have been used to derive and discuss the $^{14}N/^{15}N$ and D/H ratios: 'FIR4-west' (in red), 'FIR4-east' (in white), 'FIR4-peak' (in yellow), and 'FIR4-north' (in green). Spectra were also extracted from a region called 'FIR4-tot', which is not shown because it is the union of polygons 'FIR4-west', 'FIR4-east', and 'FIR4-peak'. *Bottom panels* (from left to right): 82-GHz continuum observed with NOEMA (Fontani et al. 2017), and N_2D^+ (2–1) averaged over the velocity range of 2.87–16.79 km s^{-1}, which includes all the hyperfine components (contours start from 2.1 mJy/beam, corresponding to the 3σ rms level of the average map, and are in steps of 6.3 mJy/beam). The map shown in the bottom right-hand panel is an enlargement of the region identified by the dashed square in the bottom left-hand panel. *In each frame*: the ellipse in the bottom left corner shows the synthesized beam (see Table 1 for the ALMA maps and Fontani et al. 2017, for the NOEMA continuum map), while the dashed circle depicts the ALMA primary beam (~68 arcsec and ~41 arcsec in bands 3 and 4, respectively). The wedge on the right indicates the range of flux density (Jy/beam). The white triangles indicate the position of the far-infrared sources FIR3, FIR4, and FIR5 (see Section 1).

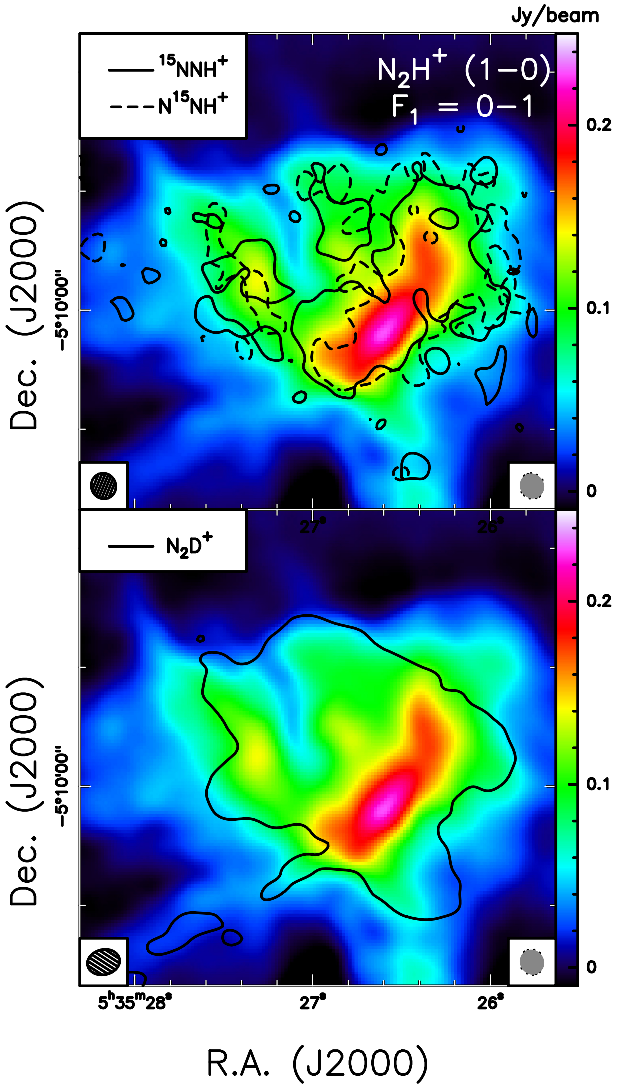

Figure 2. Top panel: solid and dashed contours show the 3σ rms level of the average maps of ^{15}NNH$^+$ and N^{15}NH$^+$ (1–0, Fig. 1), respectively, superimposed on the average emission map of the $F_1 = 0-1$ hyperfine component of N_2H^+ (colour scale). The ellipses in the bottom left and bottom right correspond to the synthesized beams of the ^{15}NNH$^+$ and N_2H^+ images, respectively. Bottom panel: same as top panel, but the depicted solid contour corresponds to the 3σ rms level of the average map of N_2D^+(2–1, Fig. 1).

components are optically thin, have the same line width, and have the same relative intensity [which indeed is ~0.1111 for all isotopologues for the considered hyperfine components, see e.g. Dore et al. (2009) for ^{15}NNH$^+$ and N^{15}NH$^+$ (1–0), and the Jet Propulsion Laboratory catalogue[3] for N_2H^+(1–0)], then the ratio between the peak flux densities of these components is equivalent to the ratios between the total flux densities of the lines. Kahane et al. (2018) compute the ^{14}N/^{15}N ratio from the total line intensity, which is, however, derived by them from the velocity-integrated intensity of the same isolated hyperfine component considered by us and also assuming optically thin conditions. Hence, if the considered hyperfine components of the different isotopologues have the same line width, and are optically thin, the methods are equivalent, and the ratios between the peak intensities of the considered hyperfine components and the total line intensities are the same.

The best-fitting peak fluxes, F_ν, of the analysed hyperfine components have been obtained with the software MADCUBA,[4] which performs a fit to the lines hyperfine structure creating a synthetic profile assuming for all components a single excitation temperature, T_{ex}, full width at half-maximum, FWHM, and separation in velocity given by the laboratory value. The software also computes the best-fitting line velocity at the intensity peak, V_p, the opacity of the various components, and the total column density of the molecule. The best-fitting F_ν are listed in Table 2, where we also give R computed in the four regions identified in Fig. 1. By comparing the 1σ rms noise level in the spectra (Table 1) with the peak intensities of the analysed hyperfine components (Table 2), we can see that the faintest hyperfine components are all detected with a signal-to-noise ratio ≥5, except for ^{15}NNH$^+$ in FIR4-east for which the signal-to-noise ratio is ~4.2.

The fits shown in Fig. 3 provide generally good results, except in some N^{15}NH$^+$ spectra in which an extra feature at ~9 km s^{-1} above 3σ in the residuals is revealed. Given that at the feature frequency (~91206.5 GHz) there are no lines of other species that can reasonably be attributed to this feature, it could be a second velocity component. However, this feature is significantly detected only in the main hyperfine component of N^{15}NH$^+$, which is not the one we use in our analysis. Close to the component used in our analysis, we never detect a significant secondary peak. Therefore, this extra feature has probably no influence on the isotopic ratios that we derive.

Fig. 4 shows the comparison between R derived in the different regions shown in Fig. 1 and that obtained by Kahane et al. (2018) with the IRAM-30m telescope: it is apparent that in OMC–2 FIR4 R does not change either from region to region or going from the single-dish scale to the interferometric scale, within the error bars. The isotopic ratios derived in each core from the two isotopologues do not show significant differences between them as well. The core in which the two values show the largest discrepancy is 'FIR4–east' (360 ± 140 and 200 ± 70 from ^{15}NNH$^+$ and N^{15}NH$^+$, respectively), but even here the two estimates are consistent within the (large) error bars.

As pointed out above, our method is based on the fact that the relative intensity of the aforementioned components with respect to the others of their hyperfine pattern is the same in all isotopologues (see e.g. Dore et al. 2009). Thus, their ratio depends only on the isotopic ratio ^{14}N/^{15}N provided that the compared hyperfine components: (1) have the same excitation temperature, (2) have the same line widths, and (3) are all optically thin.

Condition (1) is very likely because the three transitions have very similar critical densities. However, let us discuss better this approximation: from a non-Local Thermodynamic Equilibrium (non-LTE) analysis, Hily-Blant et al. (2013) found differences in T_{ex} for lines with the same quantum numbers of the different isotopologues of HCN. But these differences are in all (but one) cases below ~ 10 per cent, indicating that a significantly different T_{ex} for lines with the same quantum numbers is unlikely for isotopologues of the same species. Regarding the possibility that different hyperfine components of the same isotopologue line can

[3]https://spec.jpl.nasa.gov/ftp/pub/catalog/catform.html

[4]Madrid Data Cube Analysis on ImageJ is a software developed in the Center of Astrobiology (Madrid, INTA-CSIC) to visualize and analyse single spectra and data cubes (Martín et al. 2019; Rivilla et al. 2016).

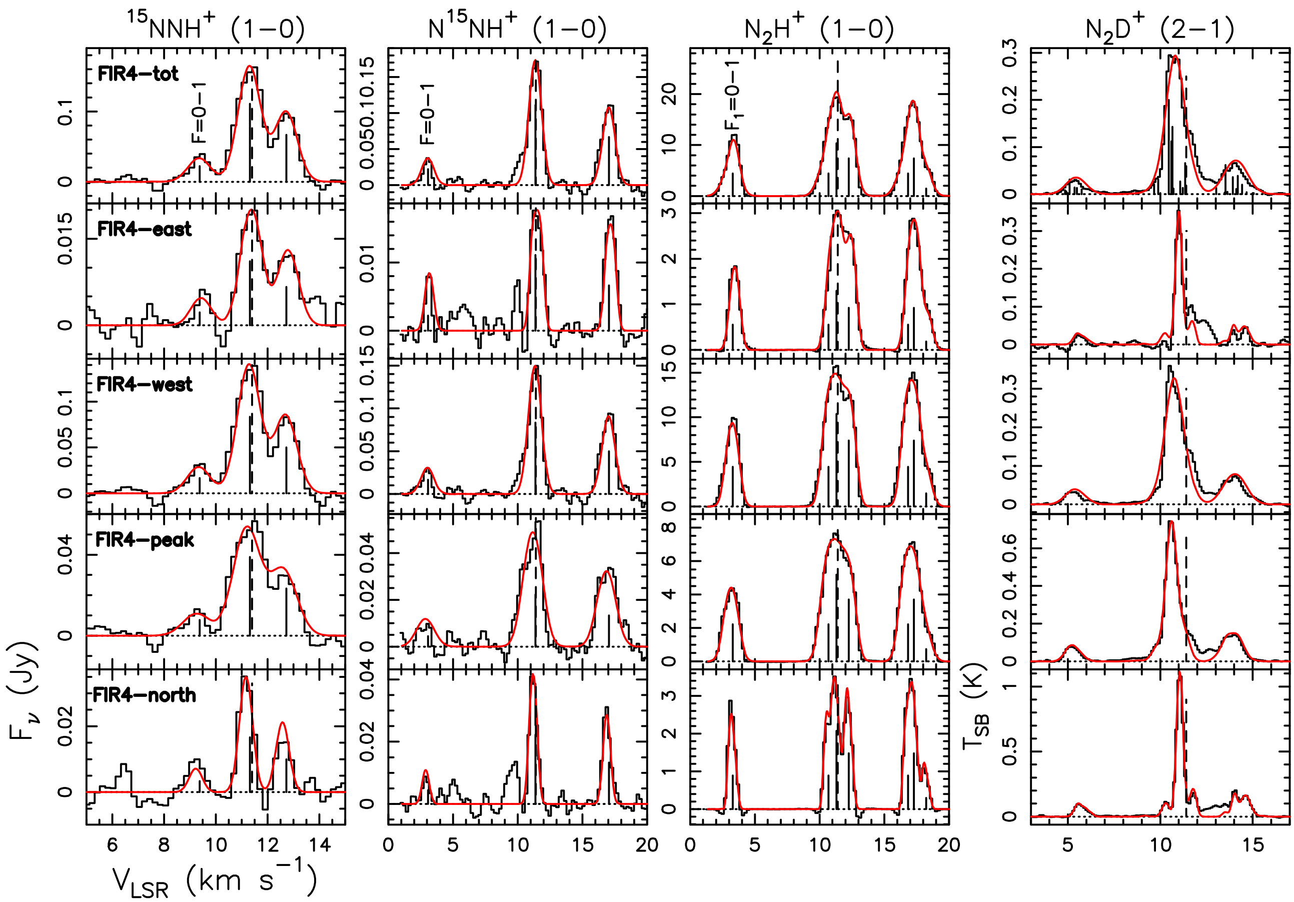

Figure 3. Spectra of, from left to right, $^{15}NNH^+$ (1–0), $N^{15}NH^+$ (1–0), N_2H^+(1–0), and N_2D^+(2–1) extracted from the five regions defined in Fig. 1, namely (from top to bottom): 'FIR4-tot', 'FIR4-east', 'FIR4-west', 'FIR4-peak', and 'FIR4-north' (see Section 4 for details). In each spectrum, the vertical dashes line indicates the systemic velocity of 11.4 km s^{-1}, and the horizontal dotted line corresponds to $y = 0$. The $^{15}NNH^+$, $N^{15}NH^+$, and N_2H^+spectra are in flux density units, because R is derived from the peak fluxes of the hyperfine components labelled in the top spectra of each column. For the $^{15}NNH^+$, $N^{15}NH^+$, and N_2H^+spectra, the red curve is the best fit to the line hyperfine structure obtained with MADCUBA, whose components are indicated by vertical, solid lines under each spectrum, the length of which is proportional to the expected relative intensity in LTE; The N_2D^+spectra are in brightness temperature (T_{SB}) units and the red curve shows the best fit obtained with MADCUBA because the parameters reported in Section 4 and Table 4 were derived from the N_2D^+spectra converted in these units (see Section 4). The hyperfine structure of N_2D^+(2–1) is shown only in the spectrum of FIR4-tot for clarity of the figure.

Table 2. Peak flux densities, F_ν, of the faintest hyperfine component in the spectra shown in Fig. 3 [$F_1 = 0$–1 of N_2H^+, and $F = 0$–1 of $^{15}NNH^+$ and $N^{15}NH^+$ (1–0)] and their ratios, R, calculated from both $^{15}NNH^+$ and $N^{15}NH^+$. F_ν has been estimated by fitting the lines with MADCUBA (Section 4.1). Their error bars include the calibration uncertainty on the absolute flux density scale of 10%, and the 1σ rms in the spectrum. This latter was computed, to be conservative, in each region from the line-free channels around each detected transition. In the uncertainties on R, calculated from the propagation of the errors, the calibration errors on F_ν cancel out because the compared spectra were calibrated in the same data cube.

Region	F_ν (Jy) N_2H^+ (1–0) $F_1 = 0$–1	F_ν (mJy) $^{15}NNH^+$ (1–0) $F = 0$–1	F_ν (mJy) $N^{15}NH^+$ (1–0) $F = 0$–1	R $^{15}NNH^+$	R $N^{15}NH^+$
FIR4-tot	11 ± 1	40 ± 10	40 ± 10	280 ± 60	280 ± 50
FIR4-east	1.8 ± 0.2	5 ± 2	9 ± 3	360 ± 140	200 ± 70
FIR4-west	10 ± 1	30 ± 10	30 ± 10	330 ± 80	330 ± 80
FIR4-peak	4.4 ± 0.5	12 ± 6	12 ± 6	370 ± 150	370 ± 150
FIR4-north	2.7 ± 0.3	8 ± 4	10 ± 5	330 ± 120	270 ± 100

have a different T_{ex}, Daniel, Cernicharo & Dubernet (2006) showed that high optical depths in N_2H^+(1–0) could indeed cause deviations from the line profile expected when each component has the same excitation temperature. According to Table 2, the optical depth of the $F_1 = 0$−1 component of N_2H^+(1–0) is in between ∼0.3 and ∼0.4, which translates into high total opacities of the lines and hence possible hyperfine 'anomalies' in their profiles. However, both theoretical (Daniel et al. 2006) and observational (Caselli,

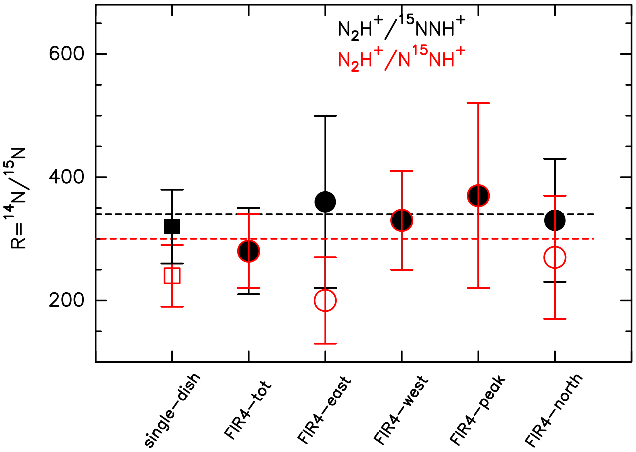

Figure 4. Isotopic ratio $R = {}^{14}N/{}^{15}N$ computed from either $^{15}NNH^+$ (black symbols) or $N^{15}NH^+$ (red symbols). The ratios have been derived for the five regions discussed in Section 4 and Fig. 1 following the method described in Section 4.1. The horizontal dashed lines correspond to the average of R in the five regions from $^{15}NNH^+$ (black) and $N^{15}NH^+$ (red). For comparison, we also show the single-dish measurements obtained by Kahane et al. (2018), squares. It is apparent that the $^{14}N/^{15}N$ ratios do not change from region to region and are all comparable to the corresponding single-dish values, within the error bars. No statistically significant differences are found between the two ^{15}N isotopologues either.

Myers & Thaddeus 1995) works show that T_{ex} of the component analysed in our work would deviate from the local thermodynamic equilibrium value by 10–15 per cent at most and only at H_2 volume densities below 10^5 cm^{-3} [see fig. 6 in Daniel et al. 2006]. Because in OMC–2 FIR4 the average H_2 volume density is 1.2×10^6 cm^{-3} (Ceccarelli et al. 2014a), where the predicted deviation from the equilibrium T_{ex} is negligible (fig. 6 in Daniel et al. 2006), we are confident that hyperfine anomalies are not affecting significantly the T_{ex} of the analysed component. This is also confirmed by the qualitative excellent agreement between data and fits (which indeed assume a single T_{ex} for all hyperfine components) for N_2H^+(1–0) in Fig. 3 around the $F_1 = 0$–1 components.

About assumptions (2) and (3), let us first discuss the $^{15}NNH^+$ and $N^{15}NH^+$ (1–0) lines. As stated above, the fit performed with MADCUBA provides several parameters, among which are V_p, FWHM, and the opacity of each hyperfine component. The tool MADCUBA-AUTOFIT provides the best-fitting parameters via a non-linear least-squared fit algorithm (see also Colzi et al. 2019). The results of these fits are shown in Table 3 and indicate that the FWHM of the two isotopologues are the same within the uncertainties, and that the optical depth of the compared components is well below 0.1. The fact that the $^{15}NNH^+$ and $N^{15}NH^+$ opacities are so low in the less-intense component is consistent with our expectations, given the low abundance of these two isotopologues. However, we stress that in some cases the uncertainties on the opacities are underestimated. In fact, as discussed in Martín et al. (2019), when one of the fit parameters in MADCUBA is fixed, then the error associated is zero, and hence the uncertainties of all quantities calculated from this parameter do not include its error. As we will illustrate in the following, sometimes we fixed T_{ex}, and hence in these cases the errors on the optical depth will be underestimated. However, the main point of this analysis is simply to confirm that the lines are optically thin, which indeed is confirmed.

For N_2H^+(1–0), for which some hyperfine components are overlapping and the line optical depth could be higher, we have performed a more accurate analysis of the line profile assuming three different T_{ex}: the best-fitting T_{ex} when leaving this parameter free, and the two extreme values of kinetic temperature measured in the envelope of OMC–2 FIR4, namely 35 and 45 K, in previous works (Ceccarelli et al. 2014a; Friesen et al. 2017). The results are shown in Tables 4–6. By comparing the parameters shown in these tables and those reported in Table 3, for each single core, we find that the N_2H^+, $^{15}NNH^+$, and $N^{15}NH^+$ lines have the same FWHM, within the uncertainties, and that the optical depth of the $F_1 = 0-1$ component is at most 0.4. Thus, conditions (2) and (3) are also satisfied.

For completeness, we have quantified the error that we make in the most unfavourable case in our simplified approach: because at most, τ of the $F_1 = 0$–1 component is 0.4 ± 0.1 for FIR4-tot, and 0.40 ± 0.08 for FIR4-west, in both cases the peak brightness temperature should be corrected by the factor $\tau/(1 - \exp(-\tau)) \sim 1.21$. For FIR4-tot, the $^{14}N/^{15}N$ ratio would change from 280 ± 60 and 280 ± 50 for $^{15}NNH^+$ and $N^{15}NH^+$, respectively, to about 340 ± 100 for both, and for FIR4-west it would change from 330 ± 80 from both $^{15}NNH^+$ and $N^{15}NH^+$ to 400 ± 120. These values are still consistent, within the uncertainties, to those derived in the other regions. Therefore, even considering the correction for the optical depth, the $^{14}N/^{15}N$ ratio does not change from region to region within the uncertainties.

4.2 D/H

We have derived the D/H ratio from the N_2H^+(1–0) and N_2D^+(2–1) lines. Due to the different quantum numbers of these transitions, we could not use the approach adopted to evaluate R. Therefore, the D/H ratio has been estimated by dividing the total column densities of $N_2D^+$and N_2H^+computed by fitting the lines with MADCUBA. We have fitted the lines with three temperatures, as explained in Section 4.1. The fits to the hyperfine structure have been performed to both $N_2H^+$and N_2D^+spectra converted

Table 3. Best-fitting peak velocities (V_p) and full widths at half-maximum (FWHM) of the ^{15}N-bearing lines obtained by fitting the hyperfine structure of the lines shown in Fig. 3 with MADCUBA (Section 4.1).

core	$^{15}NNH^+$			$N^{15}NH^+$		
	V_p km s^{-1}	FWHM km s^{-1}	$\tau_{F=0-1}$[a]	V_p km s^{-1}	FWHM km s^{-1}	$\tau_{F=0-1}$[a]
FIR4-tot	11.3 ± 0.2	1.0 ± 0.2	0.005 ± 0.002	11.4 ± 0.2	1.1 ± 0.2	0.005 ± 0.002
FIR4-east	11.4 ± 0.2	0.9 ± 0.2	0.001 ± 0.0002	11.5 ± 0.2	0.8 ± 0.2	0.001 ± 0.0002
FIR4-west	11.3 ± 0.2	1.0 ± 0.2	0.001 ± 0.0002	11.4 ± 0.2	1.1 ± 0.2	0.002 ± 0.0005
FIR4-peak	11.2 ± 0.2	1.3 ± 0.2	0.001 ± 0.0002	11.2 ± 0.2	1.5 ± 0.2	0.001 ± 0.0002
FIR4-north	11.3 ± 0.2	0.6 ± 0.2	0.003 ± 0.001	11.2 ± 0.2	0.6 ± 0.2	0.002 ± 0.0005

[a]optical depth of the $F = 0$–1 hyperfine component (see Fig. 3).

Table 4. Best-fitting line parameters of N_2H^+(1–0) and N_2D^+(2–1): in columns 2–5, we list excitation temperatures (T_{ex}), peak velocities (V_p), full widths at half-maximum (FWHM), and opacity of the $F_1 = 0-1$ hyperfine component of N_2H^+(1–0) obtained by fitting the line hyperfine structure. The fit procedure is explained in Section 4.1. In columns 6–8, we show the best-fitting V_p, FWHM, and opacity of the main hyperfine component, τ_{main}, of N_2D^+(2–1), obtained fixing T_{ex} to the value given in column 2. This was necessary, because for N_2D^+ the fit leaving T_{ex} as free parameter could not converge. The best-fitting column densities are reported in Table 7.

Core		N_2H^+				N_2D^+	
	T_{ex} K	V_p km s^{-1}	FWHM km s^{-1}	$\tau_{F_1=0-1}$	V_p km s^{-1}	FWHM km s^{-1}	τ_{main}[a]
FIR4-tot	12.5 ± 0.6	11.3 ± 0.2	1.0 ± 0.2	0.4 ± 0.1	10.6 ± 0.1	1.0 ± 0.1	0.012 ± 0.001
FIR4-east	14.6 ± 0.5	11.4 ± 0.2	0.8 ± 0.2	0.35 ± 0.07	11.0 ± 0.1	0.4 ± 0.1	0.014 ± 0.001
FIR4-west	12.3 ± 0.6	11.3 ± 0.2	1.0 ± 0.2	0.40 ± 0.08	10.8 ± 0.1	1.0 ± 0.1	0.014 ± 0.001
FIR4-peak	12.9 ± 0.9	11.2 ± 0.2	1.3 ± 0.2	0.30 ± 0.1	10.6 ± 0.1	0.7 ± 0.1	0.032 ± 0.004
FIR4-north	11.3 ± 0.4	11.2 ± 0.2	0.5 ± 0.2	0.35 ± 0.08	11.2 ± 0.2	0.4 ± 0.2	0.068 ± 0.005

[a]Optical depth of the main hyperfine component with quantum numbers $F_1 = 3-2$, $F = 4-3$ (e.g. Gerin et al. 2001), derived with MADCUBA (Section 4.2).

Table 5. Same as Table 4, fixing T_{ex} to 35 K. The best-fitting column densities are reported in Table 7.

Core		N_2H^+				N_2D^+	
	T_{ex} K	V_p km s^{-1}	FWHM km s^{-1}	$\tau_{F_1=0-1}$	V_p km s^{-1}	FWHM km s^{-1}	τ_{main}[a]
FIR4-tot	35	11.3 ± 0.2	1.2 ± 0.2	0.12 ± 0.01	10.6 ± 0.1	1.1 ± 0.1	0.003 ± 0.001
FIR4-east	35	11.4 ± 0.2	0.9 ± 0.2	0.15 ± 0.01	11.0 ± 0.1	0.4 ± 0.1	0.005 ± 0.001
FIR4-west	35	11.3 ± 0.2	1.3 ± 0.2	0.11 ± 0.01	10.8 ± 0.1	1.0 ± 0.1	0.004 ± 0.001
FIR4-peak	35	11.2 ± 0.2	1.4 ± 0.2	0.10 ± 0.01	10.6 ± 0.1	0.7 ± 0.1	0.009 ± 0.004
FIR4-north	35	11.2 ± 0.2	0.6 ± 0.2	0.15 ± 0.01	11.2 ± 0.2	0.4 ± 0.2	0.015 ± 0.005

[a]Optical depth of the main hyperfine component with quantum numbers $F_1 = 3-2$, $F = 4-3$ (e.g. Gerin et al. 2001), derived with MADCUBA (Section 4.2).

Table 6. Same as Table 4, fixing T_{ex} to 45 K. The best-fitting column densities are reported in Table 7.

Core		N_2H^+				N_2D^+	
	T_{ex} K	V_p km s^{-1}	FWHM km s^{-1}	$\tau_{F_1=0-1}$	V_p km s^{-1}	FWHM km s^{-1}	τ_{main}[a]
FIR4-tot	45	11.3 ± 0.2	1.2 ± 0.2	0.10 ± 0.01	10.6 ± 0.1	1.1 ± 0.1	0.002 ± 0.0005
FIR4-east	45	11.4 ± 0.2	0.9 ± 0.2	0.11 ± 0.01	11.0 ± 0.1	0.4 ± 0.1	0.004 ± 0.001
FIR4-west	45	11.3 ± 0.2	1.3 ± 0.2	0.08 ± 0.01	10.8 ± 0.1	1.0 ± 0.1	0.003 ± 0.001
FIR4-peak	45	11.2 ± 0.2	1.4 ± 0.2	0.08 ± 0.01	10.6 ± 0.1	0.7 ± 0.1	0.007 ± 0.002
FIR4-north	45	11.2 ± 0.2	0.6 ± 0.2	0.11 ± 0.02	11.2 ± 0.2	0.4 ± 0.2	0.012 ± 0.005

[a]Optical depth of the main hyperfine component with quantum numbers $F_1 = 3-2$, $F = 4-3$ (e.g. Gerin et al. 2001), derived with MADCUBA (Section 4.2).

in 'synthesized temperature' units. Generally, the lines are well fitted, although in all N_2D^+(2–1) spectra a residual emission partly overlapping the hyperfine pattern is apparent at ∼154.2165 GHz (right-hand panels in Fig. 3). This could be due to a contamination from the transition ($8_{4,4} - 7_{4,3}$) of CH_3CHO at 154216.68 GHz ($E_u \sim 69$ K, $S_{ij}\mu^2 = 75.9$ D^2). However, the large number of hyperfine components not contaminated by this excess emission (which, however, is always smaller than 5 per cent of the total line integrated intensity, i.e. smaller than the calibration error) allows us to well fit the hyperfine pattern in all N_2D^+spectra.

The best-fitting V_p, FWHM, and opacity of the main component of N_2D^+(2–1) are shown in Table 4, where we also give the best-fitting parameters derived for N_2H^+(1–0) already presented in Section 4.1. The best-fitting column densities are shown in Table 7 and are in the range of $\sim 0.7 - 1.7 \times 10^{14}$ cm^{-2} for N_2H^+, and $\sim 2.5 - 13.8 \times 10^{11}$ cm^{-2} for N_2D^+, which translate into D/H values in between 2.6×10^{-3} towards 'FIR4-east' and 1.4×10^{-2} towards 'FIR4-north'. We stress that, even though the total column densities in each region change by a factor of ∼1.5 assuming different excitation temperatures, the D/H ratios do not change within the uncertainties.

5 DISCUSSION AND CONCLUSIONS

Fig. 5 shows the H/D ratio against R: while H/D varies from ∼70 in 'FIR4-north' to ∼380 in 'FIR4-east', R does not. This demonstrates that there is no correlation between N and H fractionation, as also deduced by previous studies both in the same molecule (Fontani et al. 2015a) and in nitriles (Colzi et al. 2018b). Finally, it is worth noticing that the highest H/D ratio measured in 'FIR4-east' agrees with previous observations, which indicate that the eastern part of the protocluster is warmer than the western one (Fontani et al. 2017; Favre et al. 2018). On the opposite, 'FIR4-north', having the lowest H/D and located to the north-western part of the protocluster, is likely the coldest (and maybe less evolved) condensation. The D/H ratio of $N_2H^+$is a clear evolutionary indicator in low- and high-mass

Table 7. Total column densities of $N_2H^+$and $N_2D^+$and their ratio, D/H, derived fitting the spectra in Fig. 3 with MADCUBA (see Section 4.2) assuming three different T_{ex}: the best-fitting value for N_2H^+reported in Table 4, T_{ex}^{fit}, and two fixed values, 35 and 45 K, corresponding to the extrema of the kinetic temperature range estimated for the envelope of OMC–2 FIR4 by Ceccarelli et al. 2014a). We note that although the total column densities change with T_{ex} by a factor of ∼1.5, the D/H ratios are equal within the uncertainties.

Region	$N(N_2H^+)$ $\times 10^{14}(cm^{-2})$ $T_{ex}^{fit\,a}$ – 35 K – 45 K	$N(N_2D^+)$ $\times 10^{11}(cm^{-2})$ T_{ex}^{fit} – 35 K – 45 K	$\frac{D}{H} = \frac{N(N_2D^+)}{N(N_2H^+)}$ $\times 10^{-3}$ T_{ex}^{fit} – 35 K – 45 K
FIR4-tot	1.02 ± 0.05 – 1.23 ± 0.04 – 1.48 ± 0.04	4.9 ± 0.1 – 7.2 ± 0.2 – 8.5 ± 0.2	5 ± 1 – 6 ± 1 – 6 ± 1
FIR4-east	0.98 ± 0.02 – 1.23 ± 0.03 – 1.48 ± 0.03	2.5 ± 0.1 – 3.6 ± 0.2 – 4.3 ± 0.2	2.6 ± 0.5 – 2.9 ± 0.6 – 2.9 ± 0.6
FIR4-west	1.05 ± 0.06 – 1.29 ± 0.04 – 1.51 ± 0.05	5.4 ± 0.1 – 7.8 ± 0.2 – 9.3 ± 0.2	5 ± 1 – 6 ± 1 – 6 ± 1
FIR4-peak	1.10 ± 0.06 – 1.38 ± 0.05 – 1.66 ± 0.04	8.9 ± 0.1 – 12.6 ± 0.2 – 15.2 ± 0.3	8 ± 2 – 9 ± 2 – 9 ± 2
FIR4-north	0.69 ± 0.03 – 0.83 ± 0.03 – 0.98 ± 0.03	8.3 ± 0.1 – 11.5 ± 0.2 – 13.8 ± 0.3	12 ± 2 – 14 ± 3 – 14 ± 3

[a]Listed in column 2 of Table 4.

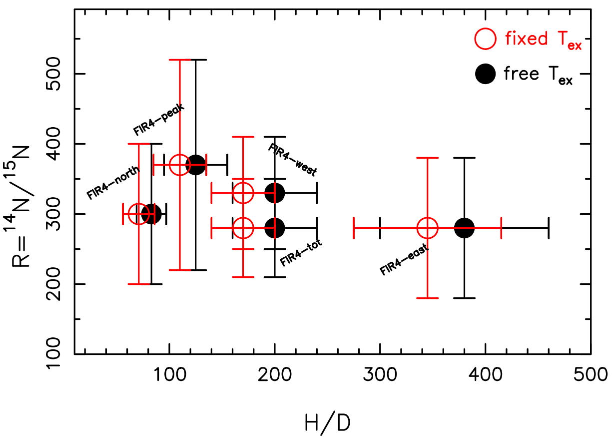

Figure 5. Comparison between the isotopic ratios $R = {}^{14}N/{}^{15}N$ and H/D listed in Tables 2 and 7, respectively, computed as explained in Sections 4.1 and 4.2. A label identifies each of the five regions defined in Section 4. We report the H/D ratios calculated by both fixing T_{ex} to 35–45 K (red symbols, the two estimates are identical within the errors) and leaving T_{ex} as a free fit parameter (black symbols).

dense cores, and it is well anticorrelated to the gas temperature (Crapsi et al. 2005; Ceccarelli et al. 2014b; Fontani et al. 2015b; De Simone et al. 2018). Therefore, our observations also demonstrate the independence of the N fractionation on the gas temperature and maybe also on the core evolutionary stage, in agreement with the most recent theoretical predictions (see Section 1).

It is interesting and useful to make a comparison with the results obtained by Colzi et al. (2019) towards the high-mass star-forming region IRAS 05358 + 3543. Colzi et al. (2019) found that R in N_2H^+shows an enhancement from ∼100–220 up to ≥200 (i.e. up to a factor of ∼2) from the core scale of ∼5 arcsec to the diffuse emission in the envelope. However, even if the two works have similar angular resolution, the distance of IRAS 05358 + 3543 (1.8 kpc) allowed Colzi et al. (2019) to resolve a linear scale of ∼0.05 pc, or ∼10 000 au. At the distance of OMC–2 FIR4, this would correspond to ∼25 arcsec, i.e. about the total N_2H^+emission size in this work. Therefore, the two works are complementary, and our results indicate that on linear scales smaller than 0.05 pc, not sampled by Colzi et al. (2019), R remains constant. To investigate if R increases from envelope to protocluster scale in OMC–2 FIR4 as found in IRAS 05358 + 3543, we have extracted spectra in different points of the envelope surrounding FIR4, in which $N_2H^+$is detected but the ${}^{15}N$ isotopologues are not, and hence derived lower limits for R in the envelope of FIR4. We have found that $R \geq 100-150$. This lower limit is smaller than the values derived in the internal part of the protocluster and hence not sufficient to put stringent constraints and unveil a possible change of R from the diffuse envelope to the dense protocluster. Therefore, a change of R from the envelope to the inner part of the protocluster as found in IRAS 05358 + 3543 cannot be ruled out.

Based on our results, the ${}^{15}N$ enrichment found in comets and protoplanetary discs (Section 1) does not seem to be inherited from the protostellar/protocluster stage, even when measured at core scales. It does not even seem to vary from the pre- to the proto-stellar stage, because the average ${}^{14}N/{}^{15}N$ ratio measured towards OMC–2 FIR4 seems also consistent with the ratios derived in pre–stellar cores (e.g. Daniel et al. 2013; Daniel et al. 2016). However, as stated in Section 1, care needs to be taken in this comparison because the ${}^{14}N/{}^{15}N$ ratio in pre-stellar cores shows a huge spread of values (of about an order of magnitude) when considering different molecules (e.g. Bizzocchi et al. 2013; Redaelli et al. 2018), the reasons of which is still not understood.

Based on our results and on the previous works in the literature, we propose hence two alternative scenarios for the ${}^{15}N$ enrichment, which, however, are not able to explain all the observational results:

(1) It occurs during the protoplanetary disc stage due to, for example, selective photodissociation of N_2, as already proposed by Guzmán et al. (2017) to explain the ${}^{15}N$ enrichment in HCN (see also Visser et al. 2018). This, however, cannot explain the ${}^{14}N/{}^{15}N$ ratio measured in TW Hya with CN, similar to the pre-stellar value (Hily-Blant et al. 2017).

(2) The enrichment occurs at different stages, depending on the molecule. For example, $N_2H^+$and HCN could be enriched at the protoplanetary disc stage.

However, limited measurements of R in protoplanetary discs and in pre- and proto-stellar objects at core scales have been performed so far. Therefore, to test both scenarios, comparative measurements of R in $N_2H^+$and other species in representatives of the different evolutionary stages of the Solar system are needed.

ACKNOWLEDGEMENTS

We thank the anonymous referee for his/her careful reading of the paper and for his/her useful comments. This work has been partially supported by the project PRIN-INAF 2016 The Cradle of Life – GENESIS-SKA (General Conditions in Early Planetary Systems for the rise of life with SKA). CC and FF acknowledge the funding from the European Research Council (ERC) under the European Union's Horizon 2020 research and innovation programme, for the Project 'The Dawn of Organic

Chemistry' (DOC), grant agreement no. 741002. LC acknowledges support from the Italian Ministero dell'Istruzione, Università e Ricerca through the grant Progetti Premiali 2012 – iALMA (CUP C52I13000140001). This paper makes use of the following ALMA data: ADS/JAO.ALMA#2016.0.00681.S. ALMA is a partnership of ESO (representing its member states), NSF (USA) and NINS (Japan), together with NRC (Canada), MOST and ASIAA (Taiwan), and KASI (Republic of Korea), in cooperation with the Republic of Chile. The Joint ALMA Observatory is operated by ESO, AUI/NRAO and NAOJ.

REFERENCES

Adams F. C., 2010, ARA&A, 48, 47
Adams J. D., et al., 2012, ApJ, 749, L24
BIzzocchi L., Caselli P., Leonardo E., Dore L., 2013, A&A, 555, 109
Bonal L., Huss G. R., Nagashima K., Krot A. N., 2009, M&PSA, 72, 5178
Caselli P., Ceccarelli C., 2012, A&ARv, 20, 56
Caselli P., Myers P. C., Thaddeus P., 1995, ApJ, 455, L77
Ceccarelli C., Dominik C., López-Sepulcre A., Kama M., Padovani M., Caux E., Caselli P., 2014a, ApJ, 790, L1
Ceccarelli C., Caselli P., Bockelée-Morvan D., Mousis O., Pizzarello S., Robert F., Semenov D., 2014b, in Beuther H., Klessen R. S., Dullemond C. P., Henning Th., eds, Protostars and Planets VI. Univ. Arizona Press, Tucson, p. 859
Chan Q. H. S., Chikaraishi Y., Takano Y., Ogawa N. O., Ohkouchi N., 2014, EP&S, 68, 7
Colzi L., Fontani F., Rivilla V. M., Sánchez-Monge Á., Testi L., Beltrán M. T., Caselli P., 2018a, MNRAS, 478, 3693
Colzi L., Fontani F., Caselli P., Ceccarelli C., Hily-Blant P., Bizzocchi L., 2018b, A&A, 609, 129
Colzi L., Fontani F., Caselli P., Leurini S., Bizzocchi L., Quaia G., 2019, MNRAS, 485, 5543
Crapsi A., Caselli P., Walmsley C. M., Myers P. C., Tafalla M., Lee C. W., Bourke T. L., 2005, ApJ, 619, 379
Daniel F., Cernicharo J., Dubernet M.-L., 2006, ApJ, 648, 461
Daniel F. et al., 2013, A&A, 560, A3
Daniel F. et al., 2016, A&A, 592, 45
De Simone M. et al., 2018, MNRAS, 476, 1982
Dore L., Bizzocchi L., Degli Esposti C., Tinti F., 2009, A&A, 496, 275
Endres C. P., Schlemmer S., Schilke P., Stutzki J., Müller H. S. P., 2016, J. Mol. Spec., 327, 95
Favre C. et al., 2018, ApJ, 859, 136
Fontani F., Caselli P., Palau A., Bizzocchi L., Ceccarelli C., 2015a, ApJ, 808, 46
Fontani F., Busquet G., Palau A., Caselli P., Sánchez-Monge Á., Tan J. C., Audard M., 2015b, A&A, 575, 87
Fontani F. et al., 2017, A&A, 605, 57
Fouchet T., Irwin P. G. J., Parrish P., Calcutt S. B., Taylor F. W., Nixon C. A., Owen T., 2004, Icarus, 172, 50
Friesen R. K. et al., 2017, ApJ, 843, 63
Füri E., Marty B., 2015, NatGe, 8, 515
Furuya K., Aikawa Y., 2018, ApJ, 857, 105
Gerin M., Pearson J. C., Roueff E., Falgarone E., Phillips T. G., 2001, ApJ, 551, L193
Guzmán V. V., Öberg K. I., Huang J., Loomis R., Qi C., 2017, ApJ, 836, 30
Henshaw J. D., Caselli P., Fontani F., Jiménez-Serra I., Tan J. C., 2014, MNRAS, 440, 2860
Hily-Blant P., Bonal L., Faure A., Quirico E., 2013, Icarus, 223, 582
Hily-Blant P., Magalhaes V., Kastner J., Faure A., Forveille T., Qi C., 2017, A&A, 603, L6
Kahane C., Jaber Al-Edhari A., Ceccarelli C., López-Sepulcre A., Fontani F., Kama M., 2018, ApJ, 852, 130
Kounkel M. et al., 2017, ApJ, 834, 142
Lichtenberg T., Golabek G. J., Burn R., Meyer M. R., Alibert Y., Gerya T. V., Mordasini C., 2019, NatAs, 3, 307
Loison J. C., Wakelam V., Gratier P., Hickson K. M., 2019, MNRAS, 484, 2747
López-Sepulcre A. et al., 2013, A&A, 556, A62
Manfroid J. et al., 2009, A&A, 503, 613
Martín S., Martín-Pintado J., Blanco-Sánchez C., Rivilla V. M., Rodríguez-Franco A., Rico-Villas S., 2019, A&A, 631, 159
Marty B., Zimmermann L., Burnard P. G., 2009, Geochim. Cosmochim. Acta, 73, 842
Marty B., Zimmermann L., Burnard P. G., Wieler R., Heber V. S., Burnett D. L., Wiens R. C., Bochsler P., 2010, GeCoA, 74, 340
Matrajt G., Messenger S., Brownlee D., Joswiak D., 2012, M&PS, 47, 525
Mezger P. G., Zylka R., Wink J. E., 1990, A&A, 228, 95
Nittler L. R., Alexander C. M.O'D., Davidson J., Riebe M. E. I., Stroud R. M., Wang J., 2018, GeCoA, 226, 107
Osorio M. et al., 2017, ApJ, 840, 36
Owen T., Mahaffy P. R., Niemann H. B., Atreya S., Wong M., 2001, ApJ, 553, L77
Pizzarello S., 2014, ApJ, 796, L25
Pizzarello S., Holmes W., 2009, GeCoA, 73, 2150
Redaelli E., Bizzocchi L., Caselli P., Harju J., Chacón-Tanarro A., Leonardo E., Dore L., 2018, A&A, 617, 7
Rivilla V. M., Fontani F., Beltrán M. T., Vasyunin A., Caselli P., Martín-Pintado J., Cesaroni R., 2016, ApJ, 826, 2
Rodgers S. D., Charnley S. B., 2008, MNRAS, 385, L48
Roueff E., Loison J. C., Hickson K. M., 2015, A&A, 576, 99
Shimajiri Y., Takahashi S., Takakuwa S., Saito M., Kawabe R., 2008, ApJ, 683, 255
Shinnaka Y., Kawakita H., Jehin E., Decock A., Hutsemékers D., Manfroid J., Arai A., 2016, MNRAS, 462, 195
Terzieva R., Herbst E., 2000, MNRAS, 317, 563
Visser R., Bruderer S., Cazzoletti P., Facchini S., Heays A. N., van Dishoeck E. F., 2018, A&A, 615, 75
Wirström E. S., Charnley S. B., 2018, MNRAS, 474, 3720
Wirström E. S., Charnley S. B., Cordiner M. A., Milam S. N., 2012, ApJ, 757, L11
Womack M., Ziurys L. M., Wyckoff S., 1992, ApJ, 387, 417
Zeng S. et al., 2017, A&A, 603, 22

This paper has been typeset from a TEX/LATEX file prepared by the author.